Intensity-dependent atomic-phase effects in high-order harmonic generation

J. Peatross* and D. D. Meyerhofer†

Laboratory for Laser Energetics, University of Rochester, 250 East River Road, Rochester, New York 14623

The far-field angular distributions of high-order harmonics of a 1054-nm laser, with orders ranging from the lower teens to the upper thirties, have been measured in thin, low-density Ar, Kr, and Xe targets. The 1.25-times-diffraction-limited, 1.4-ps-duration, Gaussian laser pulses were focused to intensities ranging from 3×10^{13} to 3×10^{14} W/cm^2, using $f/70$ optics. A gas target localized the gas distribution near the laser focus to a thickness of about 1 mm at pressures as low as 0.3 Torr. The weak focusing geometry and the low gas pressures created experimental conditions for which the harmonics could be thought of as emerging from a plane at the laser focus rather than a three-dimensional volume. The far-field distributions of nearly all of the harmonics exhibit narrow central peaks surrounded by broad wings of about the same angular divergence as the emerging laser beam. The spatial wings are due to an intensity-dependent phase variation among the dipole moments of the individual target atoms. This phase variation gives rise to broad spatial interferences in the scattered light due to the radial and temporal variation of the laser intensity.

I. INTRODUCTION

Investigations of laser high-harmonic generation in the noble gases have so far focused almost exclusively on the dependence of the harmonics on laser intensity and on propagation effects [1,2]. The extent of harmonic orders has been explored and photon energies in excess of 100 eV have been observed by a number of groups [2–6]. More recently, the dependence of harmonic generation on laser polarization has been explored [7]. Work carried out, principally by L'Huillier and co-workers [1,2,8–11], has shown that high-harmonic generation in an atomic medium can be influenced by several factors: the single-atom response to the laser field, propagation effects (phase mismatches, etc.) due to the wavelength-dependent index of refraction of both the neutral atomic and ionized media, and the geometrical propagation effects inherent to the diffraction associated with a laser focus. We report on experiments that highlight the single-atom response to the laser, via a study of the far-field profile of the emitted harmonics.

To investigate the atomic response of the medium, it is essential to characterize and minimize the propagation effects. When harmonic signals emitted from different locations in the interaction region have mismatched phases, the destructive interference not only affects the overall signal but can strongly influence the far-field distribution of the emission. This is especially true if the intensity of the driving field is above the ionization threshold of the medium. This article reports observations of high-order harmonic generation under conditions where propagation effects within the medium are unimportant, even when strong ionization occurs.

Many experiments have measured the angularly integrated harmonic emission. Angular structure can provide additional information about the harmonic-emission process. Augst et al. [12] observed the far-field angular distributions of high-order harmonics in Xe and Kr [12]. In these and, to our knowledge, all other experimental observations, the gas target pressure was at least a few torr and typically much higher. At these pressures the effects of phase mismatches caused by ionized electrons cannot be ignored. In addition, for the experiments of Augst et al. [12], the thickness of the atomic medium was on the same order as the laser confocal parameter, so that geometric propagation effects were very important to the result. It is likely that the broad, featureless forms of the far-field patterns that they observed were dominated by the effects of free electrons and the tight focusing geometry ($f/20$ optics, 1-mm gas jet). Saliéres et al. [13] recently measured far-field patterns over a much wider range of harmonics using a focusing geometry similar to that of Augst et al. [12], the results are qualitatively similar.

Tisch et al. [6] have observed the angular distribution of high-order harmonics in a few torr of He with a weaker focusing geometry ($f/50$). They have observed more sharply defined patterns, but for the very-high-order harmonics observed (up to the 91st), they report that phase mismatches from ionized free electrons play an important role in determining the harmonic far-field profile.

In contrast, we present measurements of the angular distributions of high harmonics of intermediate orders (11–41) produced with gas target pressures of less than 1 Torr. We have also employed a very weak focusing geometry ($f/70$). For our conditions and for the harmonic orders we observe, propagation effects from free electrons and from focusing geometry have a negligible effect on the harmonic far-field profiles. Thus the interpretation of the data is greatly simplified because the harmonics can be thought of as emerging from atoms lying in a plane at the laser focus rather than from a three-dimensional distribution.

The results presented in this paper are a more complete version of those presented in Ref. [14], which showed the effect of atomic dipole phase on the harmonic far-field pro-

*Also at Department of Physics and Astronomy, Unversity of Rochester, Rochester, NY 14623.
†Also at Department of Mechanical Engineering, University of Rochester, Rochester, NY 14623.

file. More recently, Salières, L'Huillier, and Lewenstein [15] have shown that the interplay between target position relative to the laser best focus and the atomic dipole phases allows a "coherence control" of the far-field profiles of the harmonics. Calculations of the effects of atomic dipole phase on the far-field profile have recently been made by Peatross, Fedorov, and Kulander [16], using dipole moments calculated for Xe from the single active electron approximation [11]. The calculations using the anharmonic oscillator model (Sec. IV B) show a very similar structure.

We produced high harmonics with a 1054-nm, 1.4-ps laser focused in Ar, Kr, and Xe. The highest observed harmonic in each gas was the 41st, 35th, and 29th, respectively. All of the harmonics had a narrow forward peak with width about one-third or less that of the laser. In addition, many of the harmonics showed broad wings surrounding the central peaks, which had an angular divergence approximately the same as the laser. The generation of the wings is attributed to an intensity-dependent phase variation in the dipole moments of the individual target atoms. Such a phase variation gives rise to broad spatial interferences in the harmonics.

This article is outlined as follows. Section II describes the experimental setup, as well as the characteristics of the laser and gas target and the capabilities and limitations of the spectrometer. Section III presents our measurements of the far-field profiles of high-order harmonics. We describe and illustrate the harmonics' dependence on the gas-target position, thickness, and pressure; on the laser intensity, polarization, and frequency; and on the atomic species. Broad wings observed in the far-field profiles of the harmonics are found to be directly connected with the atomic response to the laser field.

Section IV gives a theoretical analysis of high-order harmonic generation in a laser focus. Even though, under our conditions, the harmonics can be thought of as emerging from a plane, the analysis of Sec. IV involves a full three-dimensional picture of harmonic propagation in the focus so that our conclusions can be more strongly justified. We show that the broad wings observed in the harmonic far-field profiles can be explained by an intensity-dependent phase variation among the atomic dipoles. This is illustrated using a classical anharmonic oscillator model.

Appendix A addresses the issue of geometric propagation effects in the absence of an intensity-dependent phase variation. Our focusing parameters minimize these effects so that the far-field pattern is expected to be narrow, which is in contrast to the parameters used in other experiments [6,12,13]. Appendix B investigates the effects of ionization of the harmonic far-field patterns for our experimental conditions. We show that for our observed gas pressures and harmonic orders, ionization can play only a minor role in determining the far-field pattern.

II. EXPERIMENTAL SETUP AND CONDITIONS

An important goal of this work is to reduce propagation effects within the atomic medium so that the harmonic far-field patterns are more directly associated with the strong-field response of individual atoms. The geometrical effects of field propagation in an extended target volume and the dispersive effects of an ionized medium have been reduced as
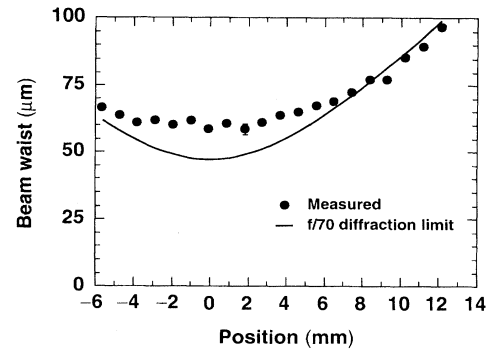

FIG. 1. Plot of the measured laser-beam waist as a function of axial position along the focus, showing that the beam is 1.25 times diffraction limited with $f/70$ optics. The solid line shows the theoretical diffraction limit.

much as possible. In addition, the laser focus was well characterized and nearly diffraction limited. Since the production of high-order harmonics can be very sensitive to the laser intensity, small aberrations in the laser beam may cause undesired distortions in the harmonic far-field pattern.

A. Laser characteristics

The laser used in these experiments is a Nd-glass, chirped-pulse amplification system, which has been described in detail elsewhere [17,18]. The wavelength of the light is 1054 nm and the pulse duration, which was monitored by autocorrelation on each shot, was 1.4 ps full width at half maximum with about 25% fluctuation. The peak laser intensities for these experiments ranged from 3×10^{13} to 3×10^{14} W/cm^2 with a measured focal area of 5500 μm^2. The laser fired a shot every 20 s. The absolute uncertainty for the laser intensity was about 50% with a relative uncertainty of 25%.

Figure 1 shows a comparison between the measured beam radius and the diffraction-limited radius of an $f/70$ beam (150-cm lens). The measured beam waist is approximately 1.25 times larger than the theoretical diffraction limit. The radius of the beam was determined by integrating over the intensity to find the effective area and then calculating the radius (to the $1/e^2$ intensity point) assuming a Gaussian distribution. The measured focal spots were nearly Gaussian and circularly symmetric. The confocal parameter of the focus as defined by the diffraction-limited curve is 13 mm.

B. Gas target

The laser intersected with a thin gas target near the focus. The target, which has been described in detail elsewhere, provided a low-density, 1-mm gas distribution [19]. The target consists of two thin metal plates separated by a small gap where gas flows. A 500-μm-diam hole drilled in the plates allows the laser to pass through and interact with the gas. The density of the gas within the hole remains relatively high, while outside the hole it disperses quickly. The gas density falls off by more than a factor of 10 at a distance of 1 mm from the hole openings. The target has been charac-
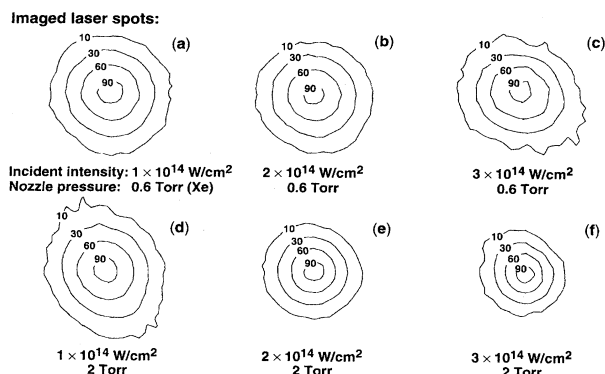
Imaged laser spots:

FIG. 2. Imaged laser focus as a function of intensity and gas-target pressure. The first row shows images with 0.6 Torr of Xe in the target and the second row shows the same scan for approximately 3 Torr.

terized experimentally [19] and the gas distribution is found to be in good agreement with Monte Carlo calculations based on free molecular flow.

A laser propagating through an ionized medium can undergo refraction due to the radial profile of the free-electron density [20]. To determine under what conditions ionization in the laser focus significantly alters the beam propagation, the laser was focused into the gas target and imaged onto a charge coupled device (CCD) camera with various pressures of Xe and various peak laser intensities. Figures 2(a)–2(c), first row, show the imaged focal spot as a function of laser intensity, where the gas pressure is 0.6 Torr for increasing laser intensity. At the highest intensity the xenon is two- and possibly three-times ionized at the center of the focus. At this low pressure, the imaged focal spot is virtually identical to that observed with no gas in the target, independent of the laser intensity. When the pressure is increased to 3 Torr [second row of Figs. 2(d)–2(f)], a decrease in the imaged focal area is observed as the laser intensity increases. This is due to refraction, which increases the cone angle of the laser as it leaves the gas target. The larger emerging beam images to a smaller spot. The position of the virtual focus was determined to confirm that the laser pulse was defocusing. To avoid this distortion, the experiments presented here were performed under conditions where no significant refraction occurs. It should be pointed out that, to our knowledge, all other high-order harmonic-generation experiments have been carried out with pressures of 3 Torr or greater.
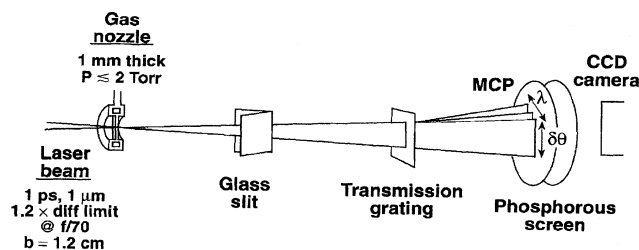

FIG. 3. Schematic of the experimental setup, including the gas target and the angularly resolved spectrometer.
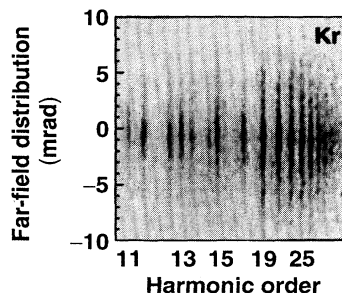

FIG. 4. Average of 20 CCD images of the angular profiles of the 11th to 35th harmonics generated in 2 Torr of Kr at 1.5×10^{14} W/cm^2.

C. Spectrometer

The harmonics produced in the gas target emerge collinearly with the laser beam. The harmonics must be spectrally resolved without the incident laser pulse damaging the spectrometer. Figure 3 shows a schematic of the spectrometer with a cutaway view of the gas target at the laser focus. Augst et al. [12] used this basic spectrometer design to observe high-harmonic far-field profiles. In our current setup, a slit is positioned approximately 30 cm behind the gas target, sampling a one-dimensional cut through the center of the laser beam (and harmonic beams). After the slit, the light passes through a gold transmission grating (either 1-μm or 0.2-μm spacing). The grating lines are oriented parallel to the slit so that the first-order diffraction of the individual harmonics is resolved after a short propagation distance.

The slit is made from two pieces of uncoated glass held at an acute angle to reduce the laser intensity on the surfaces. Glass is used rather than metal because of its higher damage threshold. The slit can be made narrow enough to cause the laser to strongly diffract, thereby reducing the energy density on the grating. There is no significant diffraction to the high harmonics because of their much shorter wavelengths. Depending on the requirements of the experiment, the slit width was varied in the range from 100 to 500 μm.

The harmonics are detected by a microchannel plate coupled to a phosphor screen (Galileo model 8081). The microchannel plate is not uv enhanced, so it cannot detect harmonics less than the ninth (177 nm). Each harmonic appears on the detector as a distinct line that reveals the harmonic angular distribution along its length. The relative energies of the different harmonic orders can also be observed. The images are recorded electronically with a CCD camera. Figure 4 shows an average of 20 images of harmonics generated in Kr as they appear at the detector. The harmonics were produced with a pressure 2 Torr and a laser intensity of 1.5×10^{14} W/cm^2. For comparison, the emerging laser beam has a $1/e^2$ radius of 7 mrad. To the sides of the lower harmonics, the second-order diffraction lines of some of the higher harmonics appear.

The spectrometer is not absolutely calibrated so that only relative levels of harmonic emission can be measured. The dynamic range (not the gain) of the detector is approximately one order of magnitude, so care must be taken to avoid saturation. The dynamic range was determined by taking advantage of a 4-μm periodic substructure running perpendicular to the line son our 0.2-μm transmission grating [21]. The
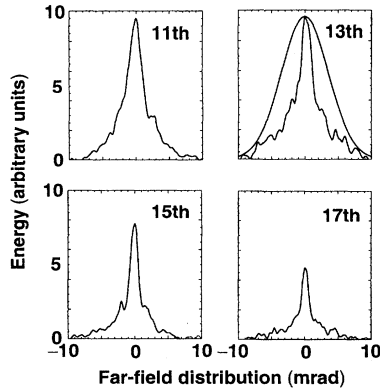
FIG. 5. Measured far-field pattern of the 11th to 17th harmonics generated in 0.3 Torr of Xe at 7×10^{13} W/cm^2. Each curve was derived from an average of 20 laser shots.

substructure causes weak ghost images of the harmonic lines to appear (~ 1 mrad above and below center in Fig. 4). Rotating the transmission grating caused the faint ghost images to appear distinctly to the sides of the principle harmonic lines. The ratio between the strength of the ghost images and the principle images is fixed and we used this to determine when the detector saturates. From this it is known that the centers of the harmonics in Fig. 4 are strongly saturated. This was done intentionally so that the wings on the harmonics could be seen easily and more harmonics would be visible.

A comparison between harmonic data taken with the 1-μm and 0.2-μm gratings revealed that our 0.2-μm grating attenuates the 11th-harmonic signal relative to the highest ones by about a factor of 4. This attenuation gradually decreases with increasing harmonic order until the harmonic orders reach the mid twenties, after which the relative efficiency is roughly constant. The fact that the 0.2-μm grating attenuates the lower harmonics is sometimes advantageous because it allows a larger number of harmonics to be seen simultaneously within the dynamic range of the detector.

III. MEASUREMENT OF HARMONIC FAR-FIELD PROFILES

We have characterized the dependences of the harmonics on various experimental parameters such as gas pressure, target position, and laser intensity. The measurements are consistent with our previous statement that, for our conditions, propagation effects within the medium play a minimal role in determining the far-field angular distribution of the harmonics.

Figure 5 shows the measured angular profiles of the 11th through 17th harmonics produced in 0.3 Torr of Xe at an intensity of 7×10^{13} W/cm^2. The curves show the harmonic far-field intensity as a function of angle. The data were obtained with the 1-μm grating with no distortions due to ghost images. Detector saturation was avoided for these data. The laser profile is depicted for comparison. The harmonics all show a narrow central peak that diminishes in width as the harmonic order increases. Each harmonic also shows broad wings, the strongest occurring on the 13th harmonic.

In principle, the harmonic far-field patterns should be cylindrically symmetric since the experimental setup is sym-
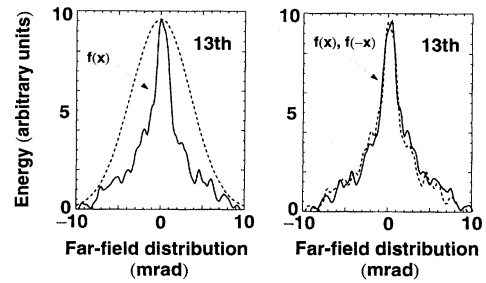

FIG. 6. The 13th harmonic from Fig. 5 plotted on top of a reflected version of itself.

metric. Therefore, any feature in the harmonic profile that does not appear on both sides of the center must be due to distortions in the laser or gas distribution, from scattered light or particles hitting the detector, or from nonuniformities in the detector itself. Figure 6 shows the 13th harmonic from Fig. 5 plotted on top of a reflected version of itself [$f(x)$ and $f(-x)$]. The noise in the data is readily apparent where the curves do not agree. However, there is good agreement between the curves for the central peak and a two-tier wing structure.

A. Dependence on gas-target parameters

The far-field angular profiles of the harmonics were investigated as a function of gas-target position relative to the laser focus. In contrast to experiments by L'Huillier and co-workers [1,2,10], who saw dramatic changes in the harmonic production with changes in gas-target position, the changes observed in these experiments were primarily due to the decrease in intensity associated with moving away from the focus. This is expected since in our case the gas distribution was much narrower than the laser confocal parameter ($l = b/13$). With the target positioned $\pm 1.7z_0$ away from the focus, where z_0 is the Rayleigh range, the far-field pattern of the harmonic profiles were qualitatively similar to those at the focus when the peak laser intensity was the same.

The relative energy $\mathscr{E}$ for a given harmonic can be found by integrating the harmonic far-field distribution, taking into account the azimuthal symmetry,

$$\mathscr{E}_{\text{total}} \propto \int_0^{\pi/2} \theta d\theta \ \mathscr{E}(\theta), \tag{1}$$
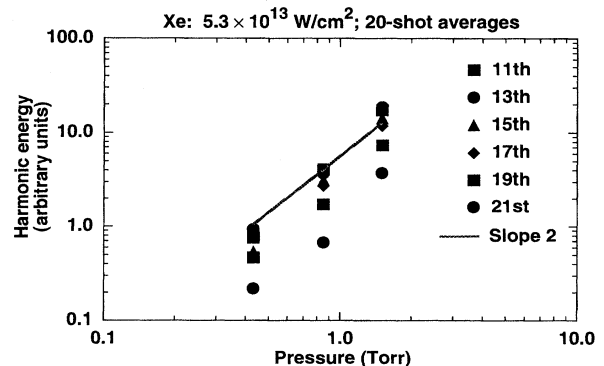

FIG. 7. Relative harmonic energy plotted as a function of target pressure of Xe at 5.3×10^{13} W/cm^2.
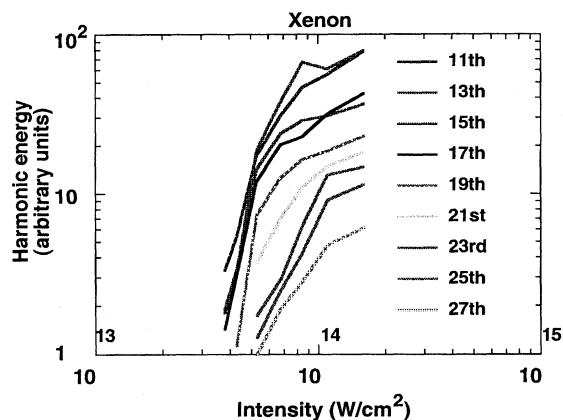
FIG. 8. Relative harmonic energy for the 11th through 27th harmonics in Xe as a function of laser intensity. The pressure has been varied to avoid detector saturation.

where θ is the angle of divergence from the z axis. The total harmonic energy is plotted in Fig. 7 as a function of target pressure in the range of our experiments. Each point is an average of 20 shots. As expected, the harmonic signal follows the square of the pressure, indicating that at these pressures, the optical index of the medium does not strongly influence the collective characteristics of the harmonic emission.

B. Dependence on laser parameters

The harmonic emission increases rapidly with laser intensity until a species-dependent saturation (not detector saturation), above which the signal increases only gradually. The harmonic saturation intensity is about 5×10^{13} W/cm^2 for Xe, 8×10^{13} W/cm^2 for Kr, and 1.5×10^{14} W/cm^2 for Ar. These intensities are roughly a factor of 2 below those where these gases strongly ionize [22,23].

Figure 8 shows the relative energy in the 11th through 27th harmonics generated in Xe as a function of laser intensity. Each point along the curve is a 20-shot average. Higher gas pressures were used to determine the points of weaker emission. The pressure dependence was assumed to be quadratic, as shown in Fig. 7. The development of a plateau and the saturation intensity of the harmonics at the higher laser intensities are clearly evident.

Figure 9 shows far-field images of harmonics produced in Xe as a function of laser intensity. Each picture is an average of 20 images. The pressure is reduced as indicated with increasing laser intensity to avoid detector saturation (compare
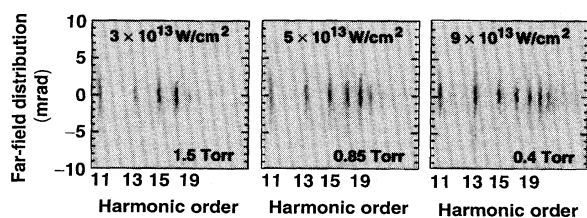

FIG. 9. Images of the angular distributions of harmonics generated in Xe as a function of laser intensity. The pressure is varied so that the signal on the detector remained roughly constant.
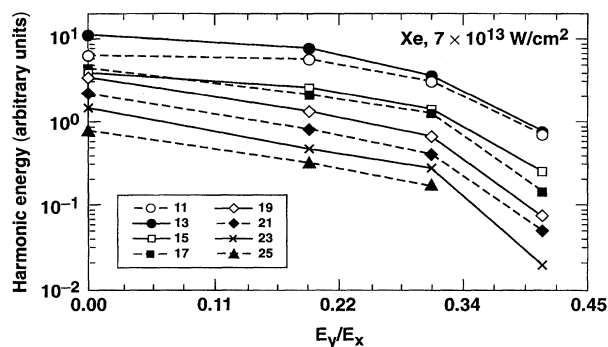

FIG. 10. Harmonic production in Xe at 7×10^{13} W/cm^2 laser intensity as a function of laser ellipticity.

with Fig. 4). The 0.2-μm grating was used to obtain this data, so the apparent intensity of the lower harmonics (orders in the teens) is reduced by approximately a factor of 4, as explained in Sec. II C. With increasing intensity, more harmonics become visible and a broad intensity-dependent wing structure becomes apparent on most harmonics. At the lower intensities, the 13th harmonic shows little if any sign of having the wing structure, while neighboring harmonics exhibit wings. However, at higher intensities, the situation reverses and the 13th harmonic shows some of the strongest wings, while the wings on the neighboring harmonics are not as strong. Similar behavior was observed in Kr and Ar.

Although the wings are typically much less intense than the central peaks, they often carry a large fraction of the total harmonic energy. Investigation of harmonic farfield profiles produced from Xe and Kr showed that the wings can contain about three times the energy as the center peaks. Clearly, the process responsible for the wings play a major role in determining the overall spatial coherence of the harmonics.

Rotating the direction of linear polarization did not affect the harmonic far-field patterns. We also studied the harmonics as a function of laser-polarization ellipticity. A quarter-wave plate placed in the laser beam introduced varying degrees of ellipticity depending on its orientation. Figure 10 shows energy of harmonics produced in Xe at 7×10^{13} W/cm^2 as a function of beam ellipticity , where the ellipticity is defined as the ratio of the peak field along the minor polarization axis to the peak field along the major polarization axis (E_y / E_x). Each point in Fig. 10 represents an average of about 20 shots. The pressure was varied to prevent detector saturation. These data are similar to that obtained by Budil et al. [7].

For the points of strongest ellipticity, we found that the harmonic production decreased more rapidly than can be explained by the simple reduction in the strength of the linear (versus circular) component of the filed. For example, the harmonic production with an ellipticity of 0.3 remained less than the production with an ellipticity of 0.2, even when the laser intensity was increased by a factor of 1.4 in the former case. We found that the details of the harmonic far-field profiles varied with ellipticity as well as with laser intensity. This is in slight disagreement with the results obtained in Ref. [7].

The laser light was frequency doubled and the resulting 527-nm beam was used to generate harmonics in Xe. The
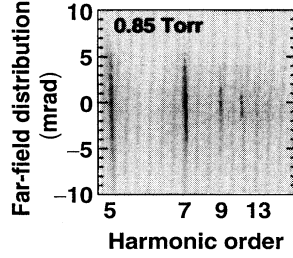
FIG. 11. Far-field image of the harmonics of green light (527 nm) produced at 1×10^{14} W/cm^2 in 0.85 Torr of Xe.

unconverted 1054-nm light was blocked with a KG3 filter. The focal-spot area of the green light was measured to be a factor of 2 smaller than that of the 1054-nm beam. For our doubling crystal, the temporal envelope of the green beam remains about the same in duration as the 1054-nm beam. Figure 11 shows the far-field pattern of the harmonics of the green light generated in Xe at 0.85 Torr at 1×10^{14} W/cm^2. The image is an average of several shots. Harmonic orders up to the 13th are clearly visible. This corresponds to the 26th harmonic of the ir laser light, which is close to the highest harmonic order seen with the ir. The harmonics of green light exhibit a wing structure similar to that from ir light.

C. Atomic species dependence

The far-field angular profiles of harmonics generated in Kr and Ar have similar behaviors to that in Xe. The development of broad wings in the far-field pattern is common to all of the gases. The detailed structure of the wings is a function of atomic species as well as harmonic order and intensity. A striking difference between the atomic species can be seen in the wing structure of the lower-order harmonics. The far-field emission for Xe, Kr, and Ar is shown in Fig. 12. Each curve is an average of four shots. For these data, the 1-μm grating was used to avoid distortions due to ghost images, though, some of the central peaks are slightly saturated. For Xe, Kr, and Ar, a prominent set of wings appears on the 13th, 15th, and 17th harmonics, respectively. These wings appear on the harmonic that is one order higher ($2\omega_L$) than the first harmonic with photon energy greater than the field-free atomic ionization potential. The shift of the pattern with atomic species is evidence that the wings are
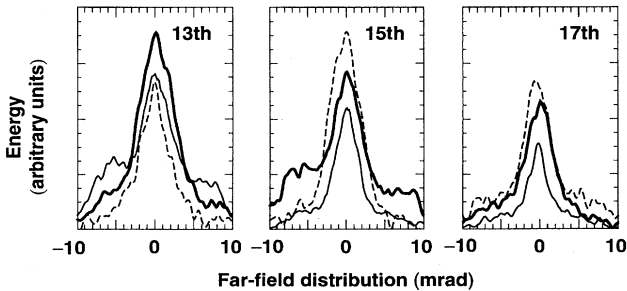

FIG. 12. The 13th, 15th, and 17th harmonics of Ar (dashed line), Kr (thin line), and Xe (thick line). The peak laser intensities were 2.1×10^{14}, 1.2×10^{14}, and 8×10^{13} W/cm^2, respectively, and the pressures were 2, 1.2, and 0.5 Torr, respectively.
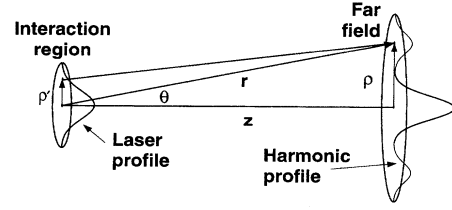

FIG. 13. Schematic depicting the propagation of laser harmonics into the far field.

a direct manifestation of atomic physics and not simply an artifact of propagation in the medium or due to phase aberrations associated with the laser focus.

IV. CALCULATIONS OF HARMONIC FAR-FIELD PROFILES EMITTED FROM A FOCUSED LASER

In this section we show calculated far-field angular profiles of harmonics emitted from a Gaussian laser focus. It is not our intention to give predictions based on accurate atomic models but rather to illustrate how various effects influence the harmonic far-field patterns. Figure 13 shows a schematic of the cylindrical coordinate system used for these calculations. In the interaction region, the spatial and temporal profile of the laser field, as well as the density distribution of the atomic medium, determines the spatial and temporal distribution of the emitted harmonic light. As the light for a given harmonic propagates to the far field, the emission from different locations combines to create the far-field angular pattern of the field. The angular pattern evolves in time according to the temporal envelope of the laser field. For these calculations, the harmonic emission is assumed to depend adiabatically on the laser-field envelope.

The harmonic field emission from each location within the interaction region must be summed to find the net contribution to each point in the far field. We assume that the emitted harmonic light does not influence the behavior of the atoms. At position $\vec{r}$ and time t in the far field, the component of the electric field that oscillates with the frequency of the qth harmonic in the Fraunhofer approximation is [1,2,11,24].

$$E_q(\vec{r},t)=\frac{eq^2\omega^2}{4\varepsilon_0c^2r}\,e^{ik_qr-iq\omega t}\int\rho'\,d\rho'\,dz'\,N_0(\rho',z',t)$$

$$\times x_q\{E_0[t-r/c]f(\rho',z')\}e^{iq\alpha(\rho',z')+i\nu_q}$$

$$\times\exp\left(-i\int_\infty^{z'}dz''\Delta(\rho',z'',t)\right.$$

$$\left.+ik_qz'\rho^2/2z2\right)J_0(k_q\rho\rho'/z)+\text{c.c.},\qquad(2)$$

where $r^2=\rho^2+z^2$. The integrals of ρ' and z' are over the interaction region near the laser focus. The integration over the azimuthal coordinate gives rise to the Bessel function J_0. N_0 is the atomic density, which depends not only on position but also on time if ionization causes significant depletion during the interaction.

The harmonic dipole moment x_q is the spatial amplitude of the component of the atomic electron motion that oscillates with the frequency of the qth harmonic. The argument of x_q is the amplitude of the laser field at the position and time of harmonic emission, where $f(\rho',z')$ is given by $[w_0/w(z')]\exp[-\rho'^2/w^2(z')]$. The phase of the harmonic at the point of production is q times the local phase of the laser plus an additional phase ν_q determined by the atomic response to the laser. The argument for ν_q is the same as that for x_q. The local phase of the laser is given by $k_1z'-\omega t+\alpha(\rho',z')$, where $\alpha(\rho',z')=k_1w_0^2\rho'^2z'/2z_0^2w^2(z')-\tan^{-1}(z'/z_0)$. The width of the Gaussian laser beam is $w(z')=w_0\sqrt{1+z'^2/z_0^2}$, where $w_0=2\lambda\,f^\#/\pi$ is the beam waist and $z_0=\pi w_0^2/\lambda$ is the Rayleigh length [25]. The $f^\#$ is the ratio of the focal length of the focusing lens divided by the beam diameter at the lens [25].

The phase term qk_1z' associated with harmonic production is not apparent in the integral because it has been canceled by a term k_qz' associated with the propagation of the harmonic light. The cancellation is approximate because, in general, the optical index of the atomic medium is different for the fundamental than for the harmonic light. The phase mismatch $\Delta k=k_q-qk_1$ depends on position through N_0 and also on time if free electrons are produced during the interaction. Hence the phase mismatch must be integrated over the focus through the position and time of harmonic production. The assumption that the propagation of the laser is unaffected by the presence of free electrons is implicit. The term $k_qz'\rho^2/2z^2$ is the phase mismatch that occurs due to the thickness of the medium for off-axis harmonic light in the far field.

The far-field pattern will evolve in time due to the temporal dependence of Eq. (2). Experimentally, we observe the total energy deposited during the entire pulse as a function of angle. Thus the profile of interest is that of the time-integrated intensity

$$\mathscr{E}(\theta)=\pi c\varepsilon_0 r^2\int dt\,|E_q(\theta,t)|^2. \tag{3}$$

Appendix A illustrates how the thickness of the gas target relative to the laser focus can strongly influence the harmonic far-field distribution for no atomic-phase dependence ($\nu_q=0$). For the illustration, a simple power law of arbitrary order is used to model the harmonic emission of the qth harmonic. It is shown that a thicker gas target can strongly broaden the far-field profiles. However, for our thin target, the harmonic far-field profiles are predicted to be much narrower than the laser and can be thought of as emerging from a plane at the focus. Appendix B examines the effect of strong ionization on the model used in Appendix A. For our gas-target pressures and for the harmonic orders that we observe, the far-field profiles are only slightly affected by ionization and they are predicted to be much narrower than the laser when the atomic phases are neglected $\nu_q=0$.

A. Effects of an intensity-dependent phase

As stated previously and demonstrated in Appendixes A and B, we have chosen experimental conditions for which propagation effects within the atomic medium are unimpor-
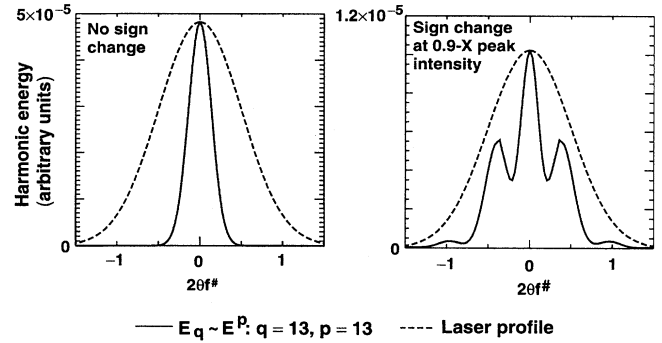

FIG. 14. Far-field pattern for the 13th harmonic where (a) ν_q does not change with laser intensity and (b) ν_q changes by π when the laser intensity goes above 90% of its peak value. The far-field pattern is plotted versus 20 f, where $f=$(focal length/diameter) of the input laser pulse.

tant in determining the harmonic far-field angular distribution. Nevertheless, our experimental data of the harmonic far-field profiles exhibit broad wings that have about the same width as the laser profile (see Fig. 5, for example). To explain the wings, we have found it necessary to postulate that the phase of the atomic dipole depends on the laser intensity through ν_q. Thus, because the laser intensity has a radial dependence, the harmonic emission from different radial positions of the interaction region can strongly interfere in the far field, creating the broad patterns we observe.

As a simple test of this idea, a harmonic far-field profile for $E_{13}=E_L^{13}$ was calculated with the harmonic dipole moment multiplied by a minus sign whenever the laser intensity was above 90% of its peak value. [In Eq. (2), ν_q was changed from 0 to π.] Other than the sign change, the emission was assumed to follow a power law according to the model of Appendix A [in Eq. (A1), $q=13$ and $p=13$]. Though our conditions are similar to that of harmonic emission from a plane, a full three-dimensional calculation was carried out. The calculation included the integration over the temporal evolution of the pulse, as in Eq. (3). Ionization effects were not included in this calculation. Figure 14(a) shows the emission pattern when the sign change is not included; Fig. 14(b) shows the emission pattern when this single sign change is included. That strong wings are caused by a phase shift is evident. This result is not sensitive qualitatively to the exact power-law order used in the calculation. For example, a similar effect can be seen by imposing a phase shift on the power law $E_{13}=E_L^5$.

B. Classical anharmonic oscillator

A strong intensity-dependent phase variation is a feature common to many high-harmonic generation models [1,4,11,26,27]. *Ab initio* calculations [11] of harmonic generation in a single xenon atom have shown strong intensity-dependent phase variations between the phase of the laser field and the phases of the emitted harmonics. Recent phase-matching calculations based on the data have demonstrated that the phase variations can scatter the harmonic light into wide angles, similar to those observed in our experiments [16]. In this section, the calculated harmonic response of an anharmonic oscillator model [28] was employed to represent

the atomic behavior for phase-matching calculations. The phase variations in the harmonic-oscillator model give results that are qualitatively similar to those of the more exact calculations [16].

The equation of motion for the anharmonic oscillation model is

$$\ddot{x} + \Gamma \dot{x} + \omega_0^2 x = F \cos\omega_L t - \beta x^3, \quad (4)$$

where β parametrizes the anharmonicity, $F = eE_0/m_e$ is a measure of the strength of the driving field, and ω_0 is the natural frequency of the oscillator when the anharmonicity is neglected. A small damping term Γ is included for convenience in the numerical calculation. The motion of the oscillator in steady state can be approximated as

$$x = \sum_q x_q \cos(q\omega_L t + \nu_q), \quad (5)$$

where x_q is the amplitude of the qth harmonic component of the motion. The oscillator is parametrized as a function of F by the values of ω_0 and β. It is appropriate to choose values for these parameters that are plausible for an atom. We chose $\hbar\omega_0$ to be the binding potential of the atom and β to fit our measurement of the third-harmonic emission as follows: For a laser intensity of 4×10^{13} W/cm^2, the values for x_3 were measured to be 5×10^{-4} Å in Ar, 2×10^{-3} Å in Kr, and 4×10^{-3} Å in Xe. Based on experimental uncertainties, we estimate the uncertainty to be a factor of 2 within the framework of the model. The parameter β is determined by requiring the solution of Eq. (4) agree with the measurement of x_3. The values for β were calculated to be 2×10^{35} (Å s)$^{-2}$ in Ar, 2×10^{35} (Å s)$^{-2}$ in Kr, and 1×10^{35} (Å s)$^{-2}$ in Xe.

To analyze Eq. (4), it is convenient to make the substitutions $x' = x\sqrt{3\beta}/\omega_L$ and $f = F\sqrt{3\beta}/2\omega_L^3$ and to rewrite the equation as

$$\sum_{-\infty}^{\infty} a_q e^{iq\omega_L t}\left(\frac{\omega_0^2}{\omega_L^2} + iq\frac{\Gamma}{\omega_L} - q^2\right) = f(e^{i\omega_L t} + e^{-i\omega_L t})$$

$$\pm\frac{1}{3}\left[\sum_{-\infty}^{\infty} a_q e^{iq\omega_L t}\right]^3, \quad (6)$$

where $x' = \sum_{-\infty}^{\infty} a_q e^{iq\omega_L t}$. The coefficients x_q in Eq. (5) are related to a_q by $x_q = 2\omega_L|a_q|/\sqrt{3\beta}$ and the intensity-dependent phase is found from $a_q = |a_q|e^{i\nu_q}$. Also, note that $a_q = a_{-q}^*$. Equation (6) can be solved under the assumption that the term a_1 is much larger than $a_{q\neq 1}$ and that a_q goes to zero for large a. This type of perturbative assumption is similar to treatments given in many nonlinear optics texts [29,30]. However, this analysis is more general than the traditional one because it allows higher-order harmonics to influence lower-order ones, which leads to the creation of a harmonic plateau. For example, after cubing the summation in Eq. (6), the non-negligible terms multiplying $e^{iq\omega_L t}$ are $3a_1^2 a_{q-2} + 6|a_1|^2 a_q + 3a_1^{*2} a_{q+2}$ for $q > 3$. The solution of Eq. (4) under this assumption is mathematically similar tot he solution to the strongly driven, two-level atom [26].
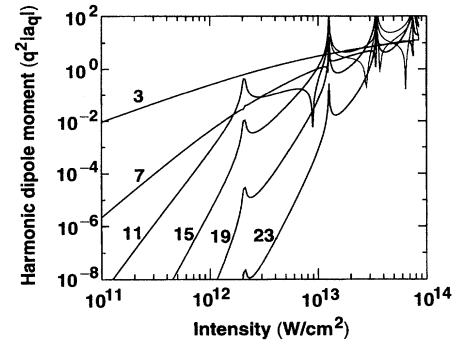

FIG. 15. Harmonic-emission curves for different harmonic orders given by an anharmonic oscillator model parametrized to Xe.

Figure 15 shows the strength (absolute value) of the harmonic emission (proportional to the oscillator acceleration) calculated by the anharmonic oscillator model with the values of ω_0 and β determined previously for Xe. The intensity range of the calculated harmonic plateau coincides with the intensity range observed experimentally. The phase of the emission (not shown in Fig. 15 slips by a factor of π around each resonance peak [ν_q of Eq. (5) changes by π].

This strong phase variation as a function of laser intensity is qualitatively similar to that seen in many models that describe high-harmonic emission [1,4,11,16,26,27]. It should be pointed out, however, that the slope of the third harmonic as calculated by the oscillator model is distinctly less than the perturbative slope, which we observed experimentally for the third harmonic at intensities in the range of the high-harmonic plateau.

The calculations involving an anharmonic oscillator are shown to illustrate the kind of behavior observed in the experiments. In particular, the phase of the dipole has a strong intensity dependence in the region of the harmonic plateau. This phase variation is sufficient to cause the broad wings observed in the far-field pattern. Figure 16 shows the far-field angular profiles of the harmonics predicted by the anharmonic oscillator for Xe. The far-field pattern is calculated using Eqs. (2) and (3). The peak laser intensity was 8.6×10^{13} W/cm^2, the value predicted by classical over-the-barrier ionization [22,23]. The effects of ionization were not included in this calculation. The calculations were performed
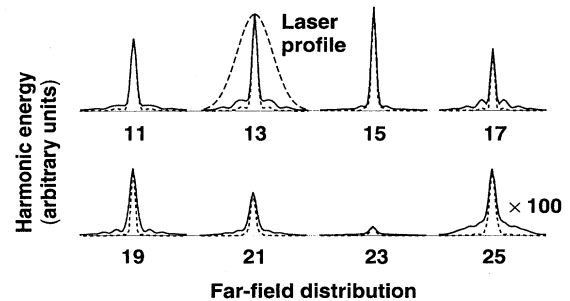

FIG. 16. Far-field harmonic angular profiles calculated with an anharmonic oscillator model for Xe (solid line). The dashed lines are calculated for the identical conditions except that the intensity-dependent phase is removed ($\nu_q = 0$).

for a three-dimensional focal volume with the target thickness chosen to match our experimental conditions ($l = b/13$).

To show that the broad wings seen in Fig. 16 are caused primarily by the intensity-dependent phase, the far-field profiles were calculated again using the absolute value of the dipole response ($\nu_q \equiv 0$). The dashed lines in Fig. 16 show the result of this calculation. The wings are significantly reduced when the intensity-dependent phase of the oscillator is ignored. The small amount of structure that remains in the wings is caused by the strong amplitude variation associated with the sharp peaks in Fig. 15.

C. Effects of a nondiffraction limited laser beam

In the previous sections the broad wings on the harmonic far-field profile have been attributed to the intensity-dependent phase of the atomic dipole response. As shown in Fig. 1, the laser focal spot was about 25% wider than the theoretical diffraction limit. It is possible that the phase errors associated with the non ideal focusing may have an effect on the far-field profile. It seems unlikely that this is an important aspect of these experiments. As mentioned above, the harmonic wing structure depends on the atomic species, on the laser intensity, and on the harmonic order (see Fig. 12). The focal characteristics of the laser are independent of these parameters and so are likely to play a minor role in the observed structure.

The far-field structure of the harmonics is related to the emission from the target medium by a Hankel transform [24]. The occurrence of broad wings in the far-field requires fine-scale structure in the near field. Images of the laser focus are shown in Fig. 2 and show little fine-scale structure. If one were to imagine that the broad wings in Fig. 6 arise from enhanced 13th harmonic emission due to a distortion in the laser focal spot, such a distortion would need to be spatially narrow (for example, ~ 13 times narrower than the laser spot). This seems unlikely for two reasons.

First, the wings in the harmonic far-field pattern contain ~ 3 times more energy than the central peak and so the emission from the distortion in the focus would have to be extremely bright given that it is of small spatial extent. Even assuming a very extreme dependence of the harmonic emission laser intensity (for example, $E_{13} \sim E_L^p$, where $p > 13$), the small structure in the laser profile would need to have several tens of percent higher laser intensity than the surrounding region, which is inconsistent with Fig. 2.

Second, in order for structures of small spatial dimension to exist in the laser focus, whether the structure be an intensity fluctuation or a phase distortion, the laser energy responsible for its occurrence must have a focusing characteristic of much smaller f number than the rest of the beam (for example, ~ 13 times lower f number). Finite apertures in the laser system, including the finite size of the focusing lens, limit the smallest scale size in the focus.

The fine structure in the harmonic patterns that are not symmetric as seen in Fig. 6 may arise from distortions in the laser beam or from imperfections in the spectrometer. The fact that this nonsymmetric structure is of high spatial frequency implies that the distortions in the laser focus responsible for it are of relatively large dimension and this in agreement with the smooth laser focal spots seen in Fig. 2.

V. CONCLUSION

The experiments presented in this work are the first observation of high-order harmonics in a regime where propagation effects within the medium are unimportant. Under our conditions, the geometric effects of the depth of focus of the laser and the phase matching due to ionized free electrons does significantly affect the harmonic far-field emission patterns. The far-field pattern is expected to be narrow for our conditions if the phase of the dipole emission is independent of laser intensity. The most important finding of this work is the occurrence of broad wings in the far-field pattern of nearly every high harmonic. The wings vary markedly with harmonic order, atomic species, laser intensity, and laser ellipticity. These dependences are strong evidence that the wings are manifestations of atomic physics and not simply artifacts of propagation effects within the medium. Because the wings cannot be attributed to propagation effects within the medium, we conclude that the phase of the dipole response has a strong laser-intensity dependence. The radial variation of the laser intensity leads to a radial variation for phase of the dipole emission. Such a phase variation can cause the harmonic light to interfere in the far field, leading to broad wings in the angular profile. A strong intensity-dependent phase of the atomic dipole response is a feature common to many high-harmonic-generation models.

APPENDIX A

For low intensities, the production of the qth harmonic depends on the qth power of the laser field intensity. In this regime, it is known that the harmonics emerge as Gaussian beams that are $\sqrt{q}$ times narrower than the laser profile [10], provided the atomic density N_0 is a function only of z'. As the laser field strength increases and the plateau regime, where many harmonic orders are produced with approximately the same conversion efficiency, is reached, the production of the qth harmonic increases only gradually with the laser intensity [11]. This change can dramatically alter the far-field pattern. This appendix investigates how the far-field pattern under this scenario depends on position and thickness of the atomic medium relative to the laser focus.

To simplify the problem, the emission of the qth harmonic is assumed to follow a power law of the order of p, where $p < q$. Also, the phase of the harmonic at the point of production is assumed to be exactly q times the local phase of

the laser ($\nu_q \equiv 0$). L'Huillier' *et al.* [10,11] performed calculations based on this model to study how the harmonics propagate within the interaction region [10,11]; however, they did not show the far-field harmonic profiles.

The atomic distribution N_0 is assumed to be independent of radius ρ'. Also, the possibility of ionization is not considered, so the integration becomes free of any temporal dependence. For these assumptions, Eq. (2) can be written as

$$E_q(\vec{r},t) = \frac{eq^2\omega^2}{4\varepsilon_0 c^2 r} x_q [E_0^p(t-r/c)] e^{ik_q r - iq\omega t} \int_{z_1}^{z_2} dz' \frac{N_0(z')w_0^p}{w^p(z')} \exp\left\{ -i\left[\int_{z_1}^{z'} dz'' \Delta k(z'') + q \tan^{-1}\left(\frac{z'}{z_0}\right) - \frac{k_q \rho^2 z'}{2z^2}\right]\right\}$$

$$\times \int_0^\infty \rho' d\rho' \exp\left[-\left(\frac{p}{w^2(z')} - iq\frac{k_1 w_0^2}{2z_0^2 w^2(z')}\right)\rho'^2\right] J_0\left(\frac{k_q \rho \rho'}{z}\right) + \text{c.c.} \tag{A1}$$

For this model, the angular distribution of the harmonics is constant in time even though their amplitude varies. The radial integration of Eq. (A1) can be performed analytically [31] to yield

$$E_q(\theta,t) = \frac{eq^2 k_1 z_0 x_q [E_0^p(t-r/c)]}{4\varepsilon_0 r} e^{ik_q r - iq\omega t}$$

$$\times \int_{z_1}^{z_2} \frac{dz' N_0(z')}{p(1+z'^2/z_0^2)^{(p-1)/2}} \exp\left(i \tan^{-1} qz'/pz_0 - iq \tan z'/z_0 - i\int_{z_1}^{z'} dz'' \Delta k(z'')\right)$$

$$\times \eta e^{-(q^2/p)\eta^2(2\theta f^\#)^2} e^{iq(2\theta f^\#)^2[1-q^2\eta^2/p^2]z'/z_0}, \tag{A2}$$

where $\eta = \sqrt{[1+(z'/z_0)^2]/[1+(qz'/pz_0)^2]}$ and ρ/z has been replaced by $\sin\theta \cong \theta$. In the case of $p=q$ (lowest-order perturbation), η is equal to 1 and all terms involving θ in Eq. (A2) can be removed from the integral. This gives an angular dependence of the form $\exp[-q(2\theta f^\#)^2]$, which is a Gaussian $\sqrt{q}$ times narrower than the laser field as expected. A remarkable feature of this case is that the far-field harmonic profile is independent of the thickness of the gas distribution, though the amplitude of the harmonic emission is affected by the thickness.

For the case where $p \neq q$, the far-field angular profile can be understood analytically for a very thin target where the limits of integration are close enough to each other that the terms containing θ in Eq. (A2) do not significantly vary over the region of integration. For a thin target positioned at the focus, η is approximately 1, and for a target positioned far outside the Rayleigh range, η can be approximated as p/q. These yield far-field profiles that are, respectively, $q/\sqrt{p}$ and $\sqrt{p}$ times narrower than the laser profile. For target positions between the two limits, the thin-target approximation yields Gaussian profiles with widths that lie between the two limits.

The thin-gas-target approximation is valid near the focus when $ql/pb < 1$ and $q(2\theta f^\#)^2(1-q^2/p^2)l/b < \pi$, where l is the target thickness and $b=2z_0$ is the laser confocal parameter. Figure 17 shows harmonic far-field patterns calculated for a target of thickness $l=b/10$ positioned at the laser focus (typical of our experimental conditions). The square modulus of the integral in Eq. (A2) is calculated while leaving off the factors in front. The harmonic power-law dependence p is chosen to be 5 and the far-field pattern is calculated for different values of q. The laser profile and the prediction for a thin-target are shown for comparison. The thin-target approximation holds for $q=15$ but begins to deviate for

$q=31$. The cases for $q=63$ and 125 are repeated in Fig. 17 with a magnified scale so that the non-Gaussian structure can be clearly seen. It is important to note that for higher values of q, as the structure becomes more complex, the angular broadening relative to the thin-target prediction is still narrow.
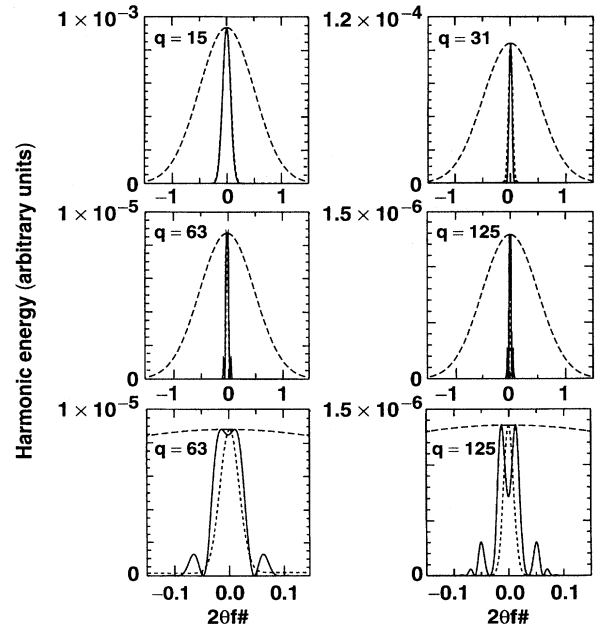

FIG. 17. Far-field profile for a thin target, $l=b/10$ for several values of q (solid line). The dashed line is the laser profile; dotted line is the prediction for the thin-target limit. For all figures $p=5$, $\Delta k=0$, and the target is positioned at the origin $z=0$. The cases for $q=63$ and 125 are repeated using a different scale.
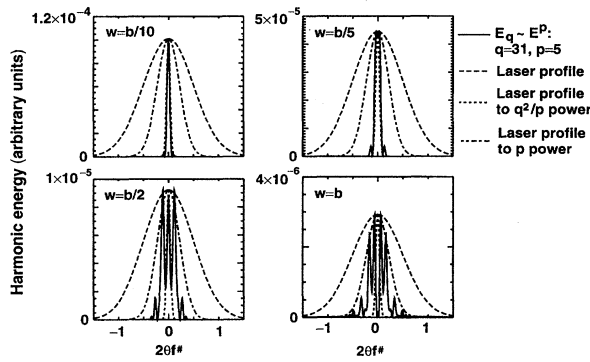
FIG. 18. Far-field profile for several target thicknesses (solid line). The dashed line is the laser profile, the dotted line is the laser profile to the pth power, and the dot-dashed line is the laser profile to the p^2/q power. For all figures $q=31$, $p=5$, $\Delta k=0$, and the target is positioned at the origin $z=0$.

Figure 18 shows the effect of target thickness on harmonics emitted from a gas target positioned at the laser focus. The harmonics become broader and a more complicated far-field profile results. The 31st harmonic is plotted for the case of $p=5$ for target thicknesses ranging from $l=b/10$ to b. In the most extreme case the curve is no wider than a Gaussian that is $\sqrt{p}$ times narrower than the laser profile. Figure 18 makes it apparent why we have chosen to prefer our experiments in a weak focusing geometry ($f/70$ optics). In this appendix we see that geometric-propagation effects within the gas medium cannot explain the broad features observed in our data.

APPENDIX B

We investigated the effects of ionization for our experimental conditions using the power-law model described in Appendix A ($q=25$, $p=5$). As the medium ionizes, the number of atoms N_0 diminishes and the value of Δk varies as the number of free electrons increases. As a result, the radial integration in Eq. (A1) cannot be performed analytically since both N_0 and Δk maintain a dependence on p'. We chose the ionization rate to follow a simple intensity
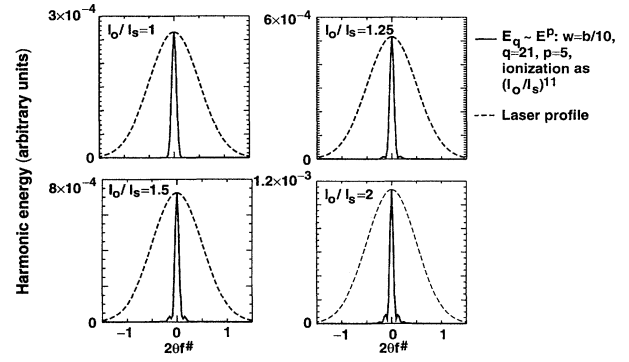

FIG. 19. Far-field pattern of the 25th harmonic calculated by Eqs. (2) and (4) for peak laser intensities below and above the ionization saturation intensity I_s. The gas density was taken at 1 Torr with a thickness of 1 mm.

power law of the order of $n=11$, as in lowest-order perturbation theory [32,33]. However, the results were not sensitive to the exact nature of the ionization rate.

Figure 19 shows far-field patterns of the 25th harmonic calculated by Eq. (A1) together with Eq. (3) for peak laser intensities at and above the ionization saturation intensity I_s. All of the factors in front of the integrals have been left off. The electron-induced phase mismatch was calculated for the typical experimental pressure of 1 Torr at 300 K with a thickness of 1 mm. The phase mismatch was taken to be $\Delta k=0$ in the neutral medium and $\Delta k=0.3\pi q$ cm^{-1} in the fully ionized medium (one electron per atom). For the higher intensities, the atoms at the center of the focus are strongly depleted during the pulse. As this occurs, the far-field pattern narrows somewhat and small wings appear. This effect is primarily due to the diffraction caused from the absence of harmonic generation in the center of the interaction region and not to phase mismatches induced by the free electrons. This can be understood when it is considered that the maximum phase mismatch of the 25th harmonic traveling 1 mm through 1 Torr of an ionized medium is only 0.7π. This is in contrast to the conditions of Tisch et al. [6], where the maximum phase mismatch for the 91st harmonic traveling 1 mm through 3 Torr of an ionized medium is 8π.

[1] Ph. Balcou and A. L'Huillier, Phys. Rev. A **47**, 1447 (1993).

[2] A. L'Huillier and Ph. Balcou, Phys. Rev. Lett. **70**, 774 (1993).

[3] N. Sarukura, K. Hata, T. Adachi, R. Nodomi, M. Watanabee, and S. Watanabee, Phys. Rev. A **43**, 1669 (1991).

[4] J. J. Macklin, J. D. Kmetec, and C. L. Gordon III, Phys. Rev. Lett. **70**, 766 (1993).

[5] C.-G. Wahlström, J. Larsson, A. Persson, T. Starczewski, S. Svanberg, P. Salières, Ph. Balcou, and A. L'Huillier, Phys. Rev. A **48**, 4709 (1993).

[6] J. W. G. Tisch, R. A. Smith, J. E. Muffett, M. Ciarrocca, J. P. Marangos, and M. H. R. Hutchinson, Phys. Rev. A **49**, R28 (1994).

[7] K. S. Budil, P. Salières, A. L'Huillier, T. Ditmire, and M. D. Perry, Phys. Rev. A **48**, R3437 (1993).

[8] A. L'Huillier, K. J. Schafer, and K. C. Kulander, Phys. Rev. Lett. **66**, 2200 (1991).

[9] A. L'Huillier, K. J. Schafer, and K. C. Kulander, J. Phys. B **24**, 3315 (1991).

[10] A. L'Huillier, P. Balcou, and L. A. Lompre, Phys. Rev. Lett. **68**, 166 (1992).

[11] A. L'Huillier, P. Balcou, S. Candel, K. J. Schafer, and K. C. Kulander, Phys. Rev. A **46**, 2778 (1992).

[12] S. Augst, D. D. Meyerhofer, J. Peatross, and C. I. Moore, in *Proceedings of the Topical Meeting on Short-Wavelength Coherent Radiation: Generation and Application*, edited by P. Bucksbaum and N. M. Ceglio (Optical Society of America, Monterey, 1991), Vol. II, p. 23.

[13] P. Salières, T. Ditmire, K. S. Budil, M. D. Perry, and A.

L'Huillier, J. Phys. B **27**, L217 (1994).

[14] J. Peatross and D. D. Meyerhofer, Phys. Rev. A **51**, R906 (1995).

[15] P. Salières, A. L'Huillier, and M. Lewenstein, Phys. Rev. Lett. **74**, 3776 (1995).

[16] J. Peatross, M. V. Fedorov, and K. C. Kulander, J. Opt. Soc. Am. B **12**, 863 (1995).

[17] P. Maine, D. Strickland, P. Bado, M. Pessot, and G. Mourou, IEEE J. Quantum Electron. **24**, 398 (1988).

[18] Y.-H. Chuang, D. D. Meyerhofer, S. Augst, H. Chen, J. Peatross, and S. Uchida, J. Opt. Soc. Am. B **8**, 1226 (1991).

[19] J. Peatross and D. D. Meyerhofer, Rev. Sci. Instrum. **64**, 3066 (1993).

[20] S. C. Rae, Opt. Commun. **97**, 25 (1993).

[21] M. L. Schattenburg, E. H. Anderson, and H. I. Smith, Phys. Scr. **41**, 13 (1990).

[22] S. Augst, D. Strickland, D. D. Meyerhofer, S. L. Chin, and J. H. Eberly, Phys. Rev. Lett. **63**, 2212 (1989).

[23] S. Augst, D. D. Meyerhofer, D. Strickland, and S. L. Chin, J. Opt. Soc. Am. B **8**, 858 (1991).

[24] J. W. Goodman, *Introduction to Fourier Optics* (McGraw-Hill, New York, 1988).

[25] P. W. Milonni and J. H. Eberly, *Lasers* (Wiley, New York, 1988).

[26] L. Plaja and L. Rosa, J. Mod. Opt. **40**, 793 (1993).

[27] K. C. Kulander, K. J. Schafer, and J. L. Krause, in *Atoms in Intense Radiation Fields*, edited by M. Gavrila (Academic, New York, 1992).

[28] A. L'Huillier, L. A. Lompré, G. Mainfray, and C. Manus, in *International Conference on Multiphoton Processes V*, edited by G. Mainfray and P. Agostini (CEA Sacley, Paris, 1990), p. 45.

[29] N. Bloembergen, *Nonlinear Optics: A Lecture Note and Reprint Volume*, 2nd ed. (Benjamin, Reading, MA, 1977), Vol. 21.

[30] R. W. Boyd, *Nonlinear Optics* (Academic, San Diego, 1992).

[31] I. S. Gradshteyn and I. M. Ryzhik, in *Tables of Integrals, Series, and Products*, edited by A. Jeffrey (Academic, New York, 1980).

[32] N. B. Delone and V. P. Krainov, in *Atoms in Strong Light Fields*, edited by V. Goldandskii, R. Gomer, F. P. Schafer, and J. P. Toennies, Springer Series in Chemical Physics Vol. 28 (Springer-Verlag, Berlin, 1985), p. 28.

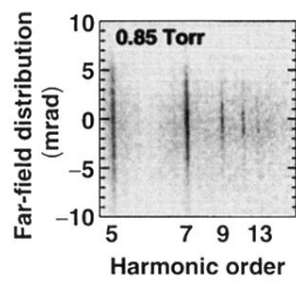[33] N. B. Delone and V. P. Krainov, *Fundamentals of Nonlinear Optics of Atomic Gases* (Wiley, New York, 1988).

FIG. 11. Far-field image of the harmonics of green light (527 nm) produced at 1×10^{14} W/cm^2 in 0.85 Torr of Xe.
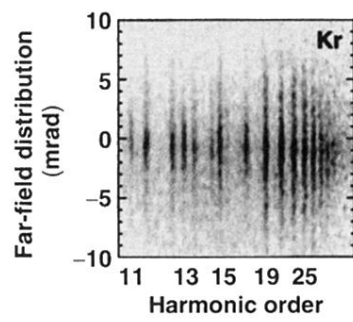
FIG. 4. Average of 20 CCD images of the angular profiles of the 11th to 35th harmonics generated in 2 Torr of Kr at 1.5×10^{14} W/cm^2.
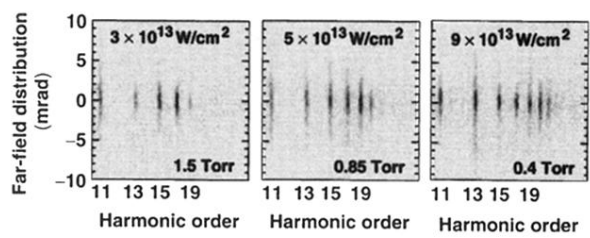
FIG. 9. Images of the angular distributions of harmonics generated in Xe as a function of laser intensity. The pressure is varied so that the signal on the detector remained roughly constant.